PHILOSOPHICAL TRANSACTIONS A

royalsocietypublishing.org/journal/rsta

Research

Article submitted to journal

Subject Areas:
Geophysics, Hydrology, Fluid Dynamics

Keywords:
induced seismicity, aseismic slip, pressure diffusion, dilatancy

Author for correspondence:
Eric M. Dunham
e-mail: edunham@stanford.edu

Fluid-driven aseismic fault slip with permeability enhancement and dilatancy

Eric M. Dunham[1,2]

[1]Department of Geophysics, Stanford University
[2]Institute for Computational and Mathematical Engineering, Stanford University

Injection-induced seismicity and aseismic slip often involve the reactivation of long-dormant faults, which may have extremely low permeability prior to slip. In contrast, most previous models of fluid-driven aseismic slip have assumed linear pressure diffusion in a fault zone of constant permeability and porosity. Slip occurs within a frictional shear crack whose edge can either lag or lead pressure diffusion, depending on the dimensionless stress-injection parameter that quantifies the prestress and injection conditions. Here we extend this foundational work by accounting for permeability enhancement and dilatancy, assumed to occur instantaneously upon the onset of slip. The fault zone ahead of the crack is assumed impermeable, so fluid flow and pressure diffusion are confined to the interior, slipped part of the crack. The confinement of flow increases the pressurization rate and reduction of fault strength, facilitating crack growth even for severely understressed faults. Suctions from dilatancy slow crack growth, preventing propagation beyond the hydraulic diffusion length. Our new 2D and 3D solutions can facilitate interpretation of induced seismicity data sets. They are especially relevant for faults in initially low permeability formations, such as shale layers serving as caprock seals for geologic carbon storage, or for hydraulic stimulation of geothermal reservoirs.

THE ROYAL SOCIETY PUBLISHING

1. Introduction

The injection, extraction, and flow of fluids in Earth's subsurface alters pore pressure and the frictional strength of faults, in some cases causing faults to slip. Slip can occur seismically, in the form of earthquakes or microseismic events. But it can also occur aseismically, with slip rates remaining sufficiently low that seismic wave radiation is suppressed. There is a growing recognition of the importance of aseismic slip in subsurface energy-related applications. Aseismic slip can be beneficial for reservoir stimulation by increasing permeability to facilitate heat exchange in geoethermal applications and to increase production rates of oil and gas [1–4]. But it can also be detrimental. Aseismic slip on faults crossing wells can shear casing and impact well stability [5]. Aseismic slip is also of concern in geologic carbon storage projects, which rely on the integrity of low permeability caprocks to prevent leakage of the buoyant CO_2 plume [6,7]. These caprock layers are often shales or rely on clays to seal faults [8]. These rocks tend to have velocity-strengthening frictional properties associated with aseismic rather than seismic slip [9]. As yet another hazard, stress changes from aseismic slip can trigger seismic slip. While in many cases the triggered seismic slip occurs as a swarm of small microseismic events [10–12], it can also occur as larger and more dangerous earthquakes [13,14].

While aseismic slip is challenging to detect, there are now several cases where shallow aseismic slip has been inferred through InSAR measurements of surface deformation [15,16]. There have also been several recent shallow field experiments aimed at probing the mechanics of fluid-driven slip [17–21]. These observations, when paired with laboratory experiments, have provided constraints on the mechanisms coupling fluids and fault slip.

Among the processes controlling the stability and style of slip and its coupling to pore pressure diffusion and fluid flow are dilatancy and permeability enhancement. Dilatancy refers to an inelastic porosity increase that, if occurring under relatively undrained conditions, reduces pore pressure. These suctions stabilize slip by increasing frictional strength. Dilatancy has been measured in many laboratory experiments [22–28]. Laboratory experiments also reveal changes in permeability from slip [29–32]. Dilatancy and permeability enhancement have also been observed in the shallow field experiments. Permeability increases from slip of one to two orders of magnitude have been reported for carbonates [17,20] and by five orders of magnitude for shales [19,21].

There have also been advances in the modeling of fluid-driven aseismic slip. Models of subduction zone slow slip events have appealed to dilatancy to prevent frictional instabilities from developing into earthquakes [33,34]. Recent modeling studies have also provided interpretation of shallow field experiments [35,36] as well as reservoir-scale aseismic slip [14,37]. From a more theoretical perspective, important insights come from analytical solutions for fluid-driven aseismic slip in response to localized injection, both in 2D [35,38,39] and 3D [40], and for more idealized spring-slider models [41]. Numerical simulations have helped quantify the importance of dilatancy as a stabilizing mechanism [42–45]. Simulations accounting for permeability enhancement have demonstrated its importance in matching laboratory and field data [20,21,35]. Permeability enhancement is also central to the phenomenon of fault valving. In fault valving, fluid migration is temporarily hindered by a permeability barrier, driving a pressure increase that weakens the fault and triggers slip, with the concomitant permeability enhancement leading to a pulse of fluid discharge and depressurization. There is widespread evidence for fault valving in natural fault systems, where it has been associated with the deposition of mineral ores during rapid depressurization [46,47]. Models of fault valving have been developing using parameterized models of permeability enhancement [48].

This study continues the specific line of research developing analytical solutions for fluid-driven aseismic slip problems [35,49]. Thus far, these solutions have employed a one-way coupling from linear pore pressure diffusion, in response to point or line source injection, to aseismic slip occurring with constant friction coefficient. Fluid transport and pressure diffusion are confined to a tabular fault zone of constant width that surrounds a planar slip surface. This

idealization is motivated by the permeability structure of natural faults, which consists of a high permeability damage zone embedded in less permeable host rock [50–52]. Despite the simplified geometry, the solutions have relevance to more complex fracture network geometries [53]. Our primary contribution is the extension of the previous 2D and 3D solutions [35,49] to account for dilatancy and permeability enhancement. Both of these processes are assumed to occur instantaneously upon the commencement of slip, and thereby enter the problem through a crack edge condition in the fluid transport problem.

2. General problem formulation

Consider an arbitrarily shaped shear crack whose interior is the surface Ω, bounded by the crack edge Γ. The outward unit normal to Γ is $\hat{n}$. The crack advances at rate $\dot{a}$ in the $\hat{n}$ direction. The crack propagates along a fault zone of width w, which in this general formulation may be spatially variable but continuous. Fluid flow is confined to the interior of the crack, with the fault zone outside assumed to be impermeable in comparison. The solid bounding the fault zone is also impermeable.

(a) Fluid flow

Inside the crack, we assume linear pressure diffusion within the permeable fault zone, with the pressure change p governed by

$$\beta\phi w\frac{\partial p}{\partial t}=\nabla\cdot\left(\frac{kw}{\eta}\nabla p\right),\quad \mathbf{x}\in\Omega. \tag{2.1}$$

Here β is the sum of fluid and pore compressibility, ϕ is the porosity, k is the permeability, and η is the fluid viscosity. These parameters are regarded as constants in the linear transport theory. The specific storage is $\beta\phi$ and the hydraulic diffusivity is $\alpha=k/(\beta\phi\eta)$. All properties can vary spatially. The divergence and gradient are two-dimensional operators acting along the surface Ω. The Darcy velocity is

$$\mathbf{q}=-\frac{k}{\eta}\nabla p. \tag{2.2}$$

Outside the crack, the fault zone is impermeable so $p=0$ and $\mathbf{q}=\mathbf{0}$.

As the crack advances, fluid flows into the pore space that is unsealed by the advancing crack edge at rate

$$q=-\frac{k}{\eta}\nabla p\cdot\hat{n},\quad \mathbf{x}\in\Gamma. \tag{2.3}$$

Conservation of fluid mass requires

$$q=(\beta\phi p+\Delta\phi^p)\dot{a}, \tag{2.4}$$

where $\Delta\phi^p$ is an increment of plastic porosity that gives rise to dilatancy. The fluid influx q can be accommodated by elastic pore expansion and fluid compression (the first term on the right side) and inelastic pore dilatation (the second term on the right side). Equation (2.4) is the novel theoretical contribution of this work, with the remainder of the analysis devoted to exploring the consequences of this problem formulation.

(b) Permeability enhancement and the dimensionless dilatancy parameter

Permeability enhancement and dilatancy are often, but not always, related. Permeability and porosity are commonly linked through a power-law relation with an exponent around 3 [54]. Increases in porosity, from both elastic and inelastic deformation of the matrix, cause increases in permeability. Elastic porosity changes, which can be calculated from knowledge of pore compressibility, porosity, and pressure change, are of order 10^{-4} to 10^{-2} for this class of problems. Plastic porosity changes likely span a similar range. We also note that increases in plastic porosity

induce dilatant suctions ($p < 0$), and the resulting elastic porosity change is negative. Thus the two contributions to porosity change are opposing, leading to overall smaller total porosity change than from each mechanism alone [55,56]. It follows from the power-law relation that permeability changes, if arising solely from porosity changes, are generally small unless the porosity increase is at least several times the initial porosity.

Permeability can also change, independently of porosity changes, by alteration of the connectivity (or tortuosity) of the pore network. This process does not result in dilatancy. The increases in permeability by two to five orders of magnitude seen in shallow field experiments [17,19–21] possibly require changes in pore connectivity (e.g., from shear-induced changes in fracture aperture).

The main point of this discussion is to explain that the permeability enhancement and dilatancy processes in our model should be regarded as somewhat independent. In particular, there are cases where permeability enhancement can occur with negligible dilatancy. One striking example is provided by a shallow injection experiment in shale, for which no dilatant suctions are seen in a monitoring borehole at the onset of slip, despite a permeability increase of five orders of magnitude [21].

In our model, the dimensionless measure of dilatancy is $\epsilon = \Delta\phi^p/(\beta\phi\Delta p)$, the ratio of plastic porosity change to the change in fluid content from elastic porosity change and fluid compressibility, where Δp is a problem-specific characteristic pressure change (to be specified later). Values of $\epsilon \ll 1$ indicate negligible effects of dilatancy, and the shale injection experiment [21] provides evidence for the relevance of this case. However, in other cases we expect that $\epsilon \gtrsim 1$. Measurements of plastic porosity changes at the field scale are limited, but it seems plausible from laboratory experiments [22,25,26] that $\Delta\phi^p$ could reach or even exceed 10^{-2}. If the change in fluid content remains small, for example because the pressure change is small, then ϵ could reach values of 10 or even 100. For example, $\epsilon = 10$ for $\beta = 10^{-8}$ Pa^{-1}, $\phi = 0.1$, $\Delta\phi^p = 10^{-3}$, and $\Delta p = 0.1$ MPa. We explore values of ϵ up to 100 in this work.

(c) Overview of two fluid-driven slip problems

In the following sections, we solve two initial value problems. Both involve crack propagation in a homogeneous whole space along the plane $z = 0$ with a tabular fault zone of constant width w. The specific storage $\beta\phi$, mobility k/η, and plastic porosity change $\Delta\phi^p$ are also constant.

The solid around the crack responds to deformation about a prestressed reference configuration in a linear elastic manner. The initial shear and effective normal stresses, τ_0 and σ_0', are constant. The initial shear stress acts in only one direction, which coincides with the direction of slip, δ. Slip occurs at constant friction coefficient f, and without cohesion, such that the shear stress τ and effective normal stress $\sigma' = \sigma_0' - p$ are related, within the crack, by $\tau = f\sigma'$. Ahead of the crack, $\tau < f\sigma'$. Stresses at the crack edge are assumed to be nonsingular with propagation occurring under the zero toughness or zero fracture energy limit (i.e., the stress intensity factors and energy release rate at the edge are zero).

The first problem is for constant pressure injection in 2D from a line source, with slip occurring under either antiplane shear or plane strain conditions. The second problem is for constant rate injection in 3D from a point source. For the 3D problem we restrict attention to Poisson's ratio equal to zero, for which the crack is circular. Both of these problems feature self-similar solutions and the derivations closely follow Bhattacharya & Viesca [35] and Sáez et al. [49].

3. 2D constant pressure injection

This is a 2D model with line source injection at constant pressure. The crack occupies the strip $-a(t) < x < a(t)$. The solution is symmetric about the injection location $x = 0$, so the problem is posed for $x > 0$ with injection specified as a boundary condition at $x = 0$. Inside the crack, the

pressure change $p(x,t)$ obeys the linear diffusion equation

$$\beta\phi\frac{\partial p}{\partial t}=\frac{k}{\eta}\frac{\partial^2 p}{\partial x^2},\quad |x|<a(t). \tag{3.1}$$

Outside of the crack ($|x|>a(t)$), $p=0$. We start with $p(x,0)=0$ and $a(0)=0$ and injection commences at $t=0$ with pressure held constant at the injector: $p(0,t)=\Delta p$.

Solution of the elasticity problem provides the stress intensity factor at the crack tips [57]:

$$K(t)=\sqrt{\frac{a(t)}{\pi}}\int_{-a(t)}^{a(t)}\frac{\tau_0-f\sigma_0'+fp(x,t)}{\sqrt{a(t)^2-x^2}}dx. \tag{3.2}$$

We assume $K=0$ at the crack tips so that stress remains finite and the energy release rate is zero.

The solution is self-similar and of diffusive character, so we write $a(t)=\lambda\sqrt{4\alpha t}$ for some λ to be determined. The pressure change is $p(x,t)=\Delta p g(\xi)$ for some dimensionless function $g(\xi)$, where $\xi=x/a(t)$ is the similarity variable.

With this change of variables, the diffusion equation (3.1) is

$$g''(\xi)+2\lambda^2\xi g'(\xi)=0 \tag{3.3}$$

and the boundary conditions corresponding to constant pressure injection and the crack edge condition (2.4) are

$$g(0)=1,\quad g'(1)+2\lambda^2\left[g(1)+\epsilon\right]=0. \tag{3.4}$$

The solution is

$$g(\xi)=\frac{1+\sqrt{\pi}\lambda e^{\lambda^2}\left[\operatorname{erf}(\lambda)-(1+\epsilon)\operatorname{erf}(\lambda\xi)\right]}{1+\sqrt{\pi}\lambda e^{\lambda^2}\operatorname{erf}(\lambda)}. \tag{3.5}$$

For small λ,

$$g(\xi)=1-2(1+\epsilon)\lambda^2\xi+O(\lambda^4). \tag{3.6}$$

The $K=0$ condition (3.2) is

$$T=\frac{2}{\pi}\int_0^1\frac{g(\xi)}{\sqrt{1-\xi^2}}d\xi, \tag{3.7}$$

where

$$T=\left(1-\frac{\tau_0}{f\sigma_0'}\right)\frac{\sigma_0'}{\Delta p}=\frac{f\sigma_0'-\tau_0}{f\Delta p} \tag{3.8}$$

is the stress-injection parameter introduced by Bhattacharya & Viesca [35]. Note that $g(\xi)$ in (3.7) depends also on λ and ϵ. Equation (3.7) can be integrated numerically (using the change of variable $\xi=\cos\theta$ to handle the integrable singularity at $\xi=1$) to obtain a relation between λ, T, and ϵ, as plotted in Figure 1. The dimensionless pressure and stress drop for several cases are shown in Figure 2. For small λ,

$$T=1-\frac{4}{\pi}(1+\epsilon)\lambda^2+O(\lambda^4). \tag{3.9}$$

Bhattacharya & Viesca [35] derived a similar solution for linear pressure diffusion everywhere on the fault (including ahead of the crack tips). Their solution is obtained by solving the diffusion equation (3.1) for all $x>0$ and replacing the crack edge condition (2.4) with $g(\xi)\to 0$ as $\xi\to\infty$. The solution is $g(\xi)=\operatorname{erfc}(\lambda\xi)$. The $K=0$ condition, equation (3.7), is identical but is evaluated using this different $g(\xi)$. This solution is also shown in Figures 1 and 2.

The relation between λ and T, in the absence of dilatancy ($\epsilon=0$), is similar to the one found by Bhattacharya & Viesca [35] for linear pressure diffusion everywhere on the fault (including ahead of the crack tips). In fact, without dilatancy, the solutions become identical when $\lambda\gg 1$. In this limit, pressure changes are limited to the region around the injector and the associated stress drop is effectively a line load in terms of its contribution to the stress intensity factor. This limiting case was studied in detail by Garagash [58].

Pronounced differences from the Bhattacharya & Viesca [35] solution arise from dilatancy, which slows the crack, in most cases leading to $\lambda<1$, even for arbitrarily small T (i.e., for faults

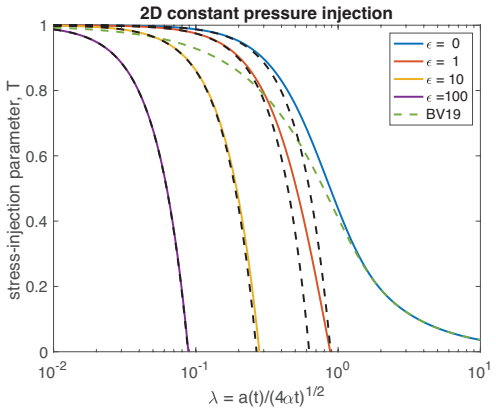

Figure 1. 2D crack with constant pressure injection. Relation between stress-injection parameter T and crack speed relative to pressure diffusion. The crack tips are located at $x = \pm a(t) = \pm\lambda\sqrt{4\alpha t}$. Dilatant suctions at the crack tips increase with ϵ, slowing the crack. The Bhattacharya & Viesca [35] solution is also shown ('BV19'). The asymptotic solution for small λ, given by (3.9), is shown as the black dashed curves.

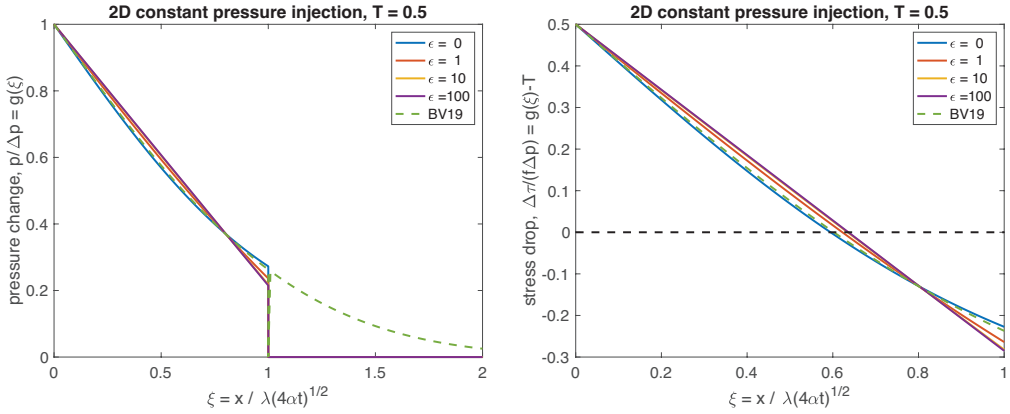

Figure 2. 2D crack with constant pressure injection. Dimensionless pressure (left) and stress drop (right) for stress-injection parameter $T = 0.5$ and various dilatancy parameters ϵ. Dilatancy slows the crack. The pressure change is identically zero ahead of the crack tip ($\xi > 1$) and is discontinuous at the tip. The Bhattacharya & Viesca [35] solution, which has nonzero pressure change ahead of the tip, is also shown ('BV19').

very close to failure). Whereas $\lambda < 1$ for the Bhattacharya & Viesca [35] model means that the crack lags the pressure diffusion front, a different interpretation is required here. This is because in our model, pressure diffusion occurs only within the crack as the fault is assumed impermeable until unsealed by the advancing crack. Thus $\lambda < 1$ means that the crack advances slower than a hypothetical pressure diffusion front would advance if the fault were everywhere permeable.

We also note that dilatancy prevents λ from diverging, even in the critically stressed ($T = 0$) limit. A closed-form expression for the maximum λ is obtained by setting $T = 0$ in equation (3.9):

$$\lambda_{\max} = \sqrt{\frac{4}{\pi(1+\epsilon)}}. \tag{3.10}$$

Because equation (3.9) is based on an asymptotic expansion for small λ, the expression above is only accurate for sufficiently large ϵ.

4. 3D constant rate injection

Next consider the 3D problem with constant rate injection. With the assumption of zero Poisson's ratio, the crack is circular [49]. Its radius is $r = a(t) = \lambda\sqrt{4\alpha t}$. The derivation is similar to the 2D constant pressure injection derivation with a few differences. The pressure diffusion equation is

$$\beta\phi\frac{\partial p}{\partial t} = \frac{k}{\eta}\frac{1}{r}\frac{\partial}{\partial r}\left(r\frac{\partial p}{\partial r}\right), \quad 0 < r < a(t). \tag{4.1}$$

The injection boundary condition is

$$\lim_{r\to 0} -2\pi r\frac{kw}{\eta}\frac{\partial p}{\partial r} = Q, \tag{4.2}$$

where Q is the injection rate (volume/time). The zero fracture energy crack growth condition is [49,59]

$$0 = \int_0^{a(t)} \frac{\tau_0 - f\sigma_0' + fp(r,t)}{\sqrt{a(t)^2 - r^2}} r dr. \tag{4.3}$$

The similarity variable is $\xi = r/a(t)$ and we define the characteristic pressure change [49]

$$\Delta p = \frac{Q\eta}{4\pi kw}. \tag{4.4}$$

The pressure change is $p(r,t) = \Delta p g(\xi)$. The pressure diffusion equation (4.1) is

$$\xi^{-1}\left(\xi g'(\xi)\right)' + 2\lambda^2\xi g'(\xi) = 0 \tag{4.5}$$

and the boundary conditions corresponding to constant rate injection (4.2) and the crack edge condition (2.4) are

$$\lim_{\xi\to 0} -\frac{\xi}{2}g'(\xi) = 1, \quad g'(1) + 2\lambda^2\left[g(1) + \epsilon\right] = 0. \tag{4.6}$$

The crack growth condition (4.3) is

$$T = \int_0^1 \frac{g(\xi)}{\sqrt{1-\xi^2}}\xi d\xi. \tag{4.7}$$

Note that while the definition of T remains the same as for the 2D problem, it can now assume values greater than unity. This is because Δp is a characteristic pressure change, not the injection pressure (the pressure around the injector has a logarithmic singularity). Later we provide expressions estimating the pressure change around the injector, which may be useful when comparing to wellhead pressure data.

The solution is

$$g(\xi) = E_1(\lambda^2\xi^2) - E_1(\lambda^2) + \lambda^{-2}e^{-\lambda^2} - \epsilon. \tag{4.8}$$

Asymptotics for small λ are

$$g(\xi) = \lambda^{-2} - 1 - \ln\xi^2 - \epsilon + O(\lambda^2) \tag{4.9}$$

and

$$T = \lambda^{-2} + 1 - \ln 4 - \epsilon + O(\lambda^2), \tag{4.10}$$

which combine to give

$$g(\xi) \approx T - 2 + \ln 4 - \ln\xi^2. \tag{4.11}$$

The solution with pressure diffusion everywhere, used by Sáez et al. [49], is

$$g(\xi) = E_1(\lambda^2\xi^2), \tag{4.12}$$

with asymptotics for small λ given by

$$g(\xi) = -\gamma - \ln\lambda^2\xi^2 + O(\lambda^2) \tag{4.13}$$

and

$$T = 2 - \gamma - \ln 4\lambda^2 + O(\lambda^2), \tag{4.14}$$

where γ is the Euler–Mascheroni constant.

Results are shown in Figures 3 and 4. The effects of permeability enhancement and dilatancy are similar to those in the 2D constant pressure injection problem. Without dilatancy ($\epsilon = 0$), the solution matches Sáez et al. [49] in the large λ limit for the same reasons as in the 2D problem (pressure changes are confined to the vicinity of the injector and the associated stress drop acts as a point load).

Dilatancy slows crack growth and ultimately provides an upper bound on λ, even for critically stressed faults ($T \to 0$). We denote the maximum λ obtained as $T \to 0$ as $\lambda_{\max}$. For $\epsilon \gtrsim 1$, $\lambda_{\max} \lesssim 1$. This warrants use of the asymptotic expansion (4.10). Setting $T = 0$ we obtain

$$\lambda_{\max} = (-1 + \ln 4 + \epsilon)^{-1/2}. \tag{4.15}$$

Thus we conclude that even a moderate amount of dilatancy ($\epsilon \gtrsim 1$) prevents the crack from ever propagating faster than a hypothetical pressure diffusion front, regardless of how close the fault is to failure or how large the injection rate is. This is a pronounced difference from the prediction of the Sáez et al. [49] model.

The behavior in the large T (severely understressed or marginally pressurized) limit is also quite different, as we explain in the following section.

However, before proceeding, we provide expressions estimating the pressure change around the injector. While the singular source injection solutions used in this and previous work feature a logarithmic singularity at $r = 0$, Sáez & Lecampion [60,61] showed that these solutions provide an excellent approximation to nonsingular solutions where fluid is injected from a wellbore of finite radius R, provided that $t \gg R^2/\alpha$. This condition is well satisfied for applications of interest. Pressure at the injector is obtained by evaluating $p(r,t) = \Delta p g(\xi)$ at $r = R$ and hence $\xi = R/(\lambda\sqrt{4\alpha t})$, or equivalently, $\lambda^2\xi^2 = R^2/(4\alpha t)$. The asymptotic expansions for small ξ, given by (4.9) for our new model and (4.13) for the Sáez et al. [49] model, can be used. For the the Sáez et al. [49] model, this gives

$$p(R,t) \approx \Delta p \left[-\gamma - \ln\left(\frac{R^2}{4\alpha t}\right)\right], \tag{4.16}$$

which Sáez & Lecampion [60,61] note is only weakly dependent on time and approximated, to order of magnitude accuracy, as $4\pi\Delta p$. For our model,

$$p(R,t) \approx \Delta p \left[\lambda^{-2} + \ln\lambda^2 - 1 - \epsilon - \ln\left(\frac{R^2}{4\alpha t}\right)\right]. \tag{4.17}$$

Making the same Sáez & Lecampion [60,61] approximation, we write this as

$$p(R,t) \approx \Delta p \left(\lambda^{-2} + \ln\lambda^2 - 1 - \epsilon + \gamma + 4\pi \right). \tag{4.18}$$

It is evident that for small λ and/or large ϵ, the pressure can be quite different from $4\pi\Delta p$.

5. Fault unsealing allows fluid-driven crack growth under severely understressed conditions

Here we discuss behavior in the large T (severely understressed or marginally pressurized) limit for the 3D constant rate injection problem. Figure 3 shows that under these conditions, the Sáez et al. [49] model predicts negligible crack growth. The pressure increase within the crack is insufficiently large to cause slip, except in the immediate vicinity of the injector. In contrast, appreciable crack growth always occurs in our model with an impermeable fault ahead of the crack edge, even under large T conditions.

Figure 5 provides an example for $T = 30$, a value that is representative of conditions in the 2012 stimulation of the Habanero 4 well in the Cooper Basin, Australia, enhanced geothermal

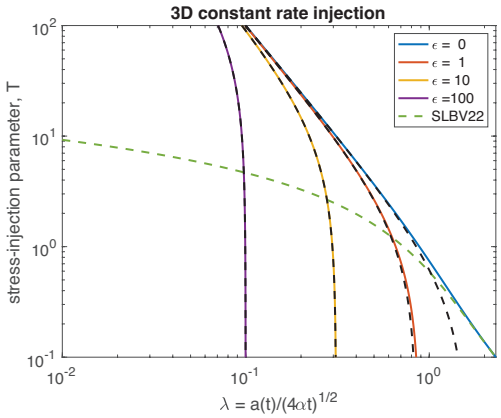

Figure 3. 3D circular crack with constant rate injection. Relation between stress-injection parameter T and crack speed relative to pressure diffusion. The crack edge is located at $r = a(t) = \lambda\sqrt{4\alpha t}$. Dilatant suctions at the crack edge increase with ϵ, slowing the crack. The Sáez et al. [49] solution is also shown ('SLBV22'). The asymptotic solution for small λ, given by (4.10), is shown as the black dashed curves.

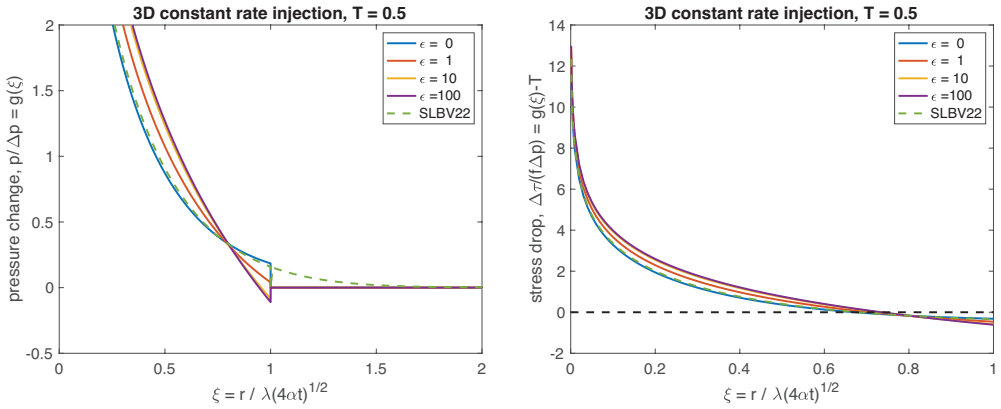

Figure 4. 3D circular crack with constant rate injection. Dimensionless pressure (left) and stress drop (right) for stress-injection parameter $T = 0.5$ and various dilatancy parameters ϵ. Dilatancy slows the crack. The pressure change is identically zero ahead of the crack edge ($\xi > 1$) and is discontinuous at the tip. The Sáez et al. [49] solution, which has nonzero pressure change ahead of the tip, is also shown ('SLBV22').

systems project (discussed further in the Discussion section). The pressure increase within the crack is considerably higher than the characteristic pressure change Δp, which is the appropriate scale of pressurization in the Sáez et al. [49] model. To investigate this further, we provide plots of pressure change for several values of T (and without dilatancy) in Figure 6. As T increases, crack growth slows and the injected fluids occupy a smaller volume. This confinement of fluid leads to greater pressurization, ultimately to the point that the slip condition is met. (It is also possible that hydraulic fracturing occurs before this.) The characteristic pressure change is $T\Delta p$, rather than Δp, in the large T limit, as shown by equation (4.11).

We can gain further insight into differences in the large T and small λ behavior for our model and the Sáez et al. [49] model by examining the asymptotic relations between T and λ, given by (4.10) and (4.14), respectively. Dilatancy is of minor importance in this limit and our model predicts $\lambda \sim T^{-1/2}$ whereas the Sáez et al. [49] model predicts a much faster (exponential) decay of λ with increasing T, namely, $\lambda \sim (1/2)e^{(2-\gamma-T)}$. Thus we conclude that the confinement of

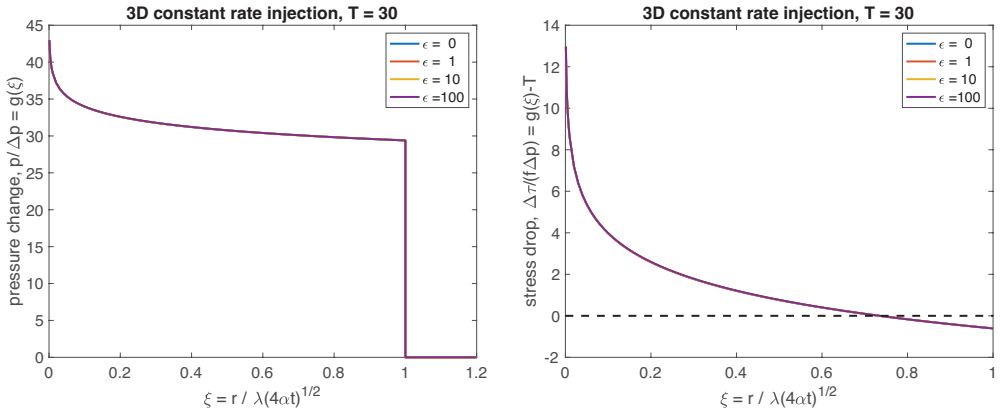

Figure 5. 3D circular crack with constant rate injection. Dimensionless pressure (left) and stress drop (right) for stress-injection parameter $T = 30$ and various dilatancy parameters ϵ. All curves are approximately identical when nondimensionalized in this manner, but λ decreases as ϵ increases. The pressure change is identically zero ahead of the crack edge ($\xi > 1$) and is discontinuous at the tip. Crack growth is effectively nonexistent in the Sáez et al. [49] model for these high T conditions.

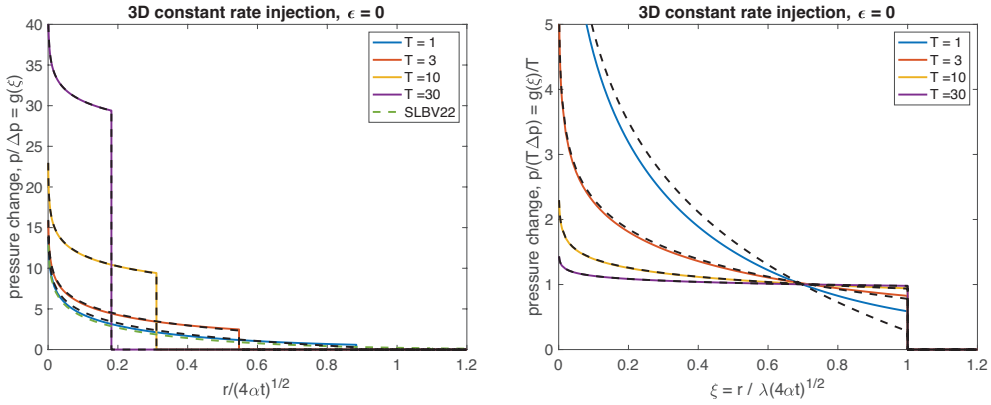

Figure 6. 3D circular crack with constant rate injection. (left) Dimensionless pressure for various values of the stress-injection parameter T, but without dilatancy ($\epsilon = 0$). Crack growth is effectively nonexistent in the Sáez et al. [49] model for large T conditions. In contrast, confinement of flow to the interior of the crack leads to increasingly large pressurization as T increases, allowing fluid-driven crack growth even for severely understressed (large T) faults. (right) Alternative nondimensionalization illustrating that the characteristic pressure increase within the crack is $T\Delta p$ in the large T limit. Dashed black curves show the asymptotic solution given in equation (4.11).

flow to the interior of the crack permits fluid-driven crack growth under a much broader range of conditions than had previously been recognized.

6. Discussion

Here we discuss the relevance of our 2D and 3D solutions to several applications involving subsurface fluid injection. The first application comes from the Cooper Basin, Australia, enhanced geothermal systems project targeting hot granites at approximately 4 km depth [62]. The project was ultimately canceled after it was recognized that rather than stimulating a large volume, injection was largely confined to the $w = 6$ m wide damage zone of the Habanero fault. Injection

and pressure diffusion along this fault triggered microseismic swarms that migrated outward from the injection wells during stimulation treatments [63–66]. Borehole measurements of stress and pore pressure for this subhorizontal thrust fault [67,68] yield $\tau_0 \approx 9.06$ MPa and $\sigma_0' \approx 26.4$ MPa (and hence $\tau_0/\sigma_0' \approx 0.34$, much less than a typical friction coefficient for granite of $f = 0.6$). For the 2012 stimulation of the Habanero 4 well, the representative injection rate was $Q = 25$ L/s [65,66,69]. Taking $k = 10^{-12}$ m^2, $\eta = 8 \times 10^{-4}$ Pa s, and $f = 0.5$, the characteristic pressure change from (4.4) is $\Delta p \approx 0.27$ MPa and the stress-injection parameter is $T \approx 31$. This is in the severely understressed limit, for which the Sáez et al. [49] model predicts negligible fluid-driven crack growth. This is in contrast to the observed cloud of microseismicity, which migrates outward by 500 m over 7 days. As discussed in the previous section, the relevant pressure change from our solution, which assumes that pressurization is confined to the slipped crack interior, is $T\Delta p \approx 8.3$ MPa We next estimate the specific storage as $\beta\phi = 5 \times 10^{-10}$ Pa^{-1} [62], giving a hydraulic diffusivity of $\alpha = 2.5$ m^2/s. Assuming $\epsilon = 0$ (no dilatancy), we obtain $\lambda \approx 0.18$. (Results are nearly the same with dilatancy provided that $\epsilon \lesssim 10$, as is evident from Figure 3.) After 7 days of injection, the crack edge is predicted to have advanced outward about 440 m. This is reasonably consistent with the observed position of the seismicity front. Furthermore, the predicted pressure change at the well is about 12 MPa, which is similar to but slightly higher than the measured pressure change of about 10 MPa [65,66]. Further parameter adjustments, within the uncertainties of the measurements, might bring the model into even more consistency with the observations. We also note that despite the large T value, the pressure change is still only half of what would be required for pressure to reach the minimum principal stress and initiate hydraulic fracturing. Overall, this exercise demonstrates how the model can be used to interpret observations of fluid-driven slip.

Of course, our solution is for aseismic slip by virtue of the constant friction coefficient assumption, whereas the observed slip was seismic. We speculate that the general features predicted by our model, specifically the diffusive expansion of a pressurized zone with slip confined within it, carry over to the seismic case (at least if stress conditions prohibit runaway rupture [40,70,71]). For velocity-weakening friction with sufficiently small nucleation length, as compared to the spatial extent of the pressurized and slipped region, we anticipate that slip will take the form of small microseismic events. Simulations are required to test this hypothesis.

Our solution might be relevant also for assessing the integrity of caprock seals on reservoirs used for carbon storage through CO_2 injection. As a specific example, Silva et al. [8] discuss the viability of storage in sedimentary basins in the Gulf of Mexico. The proposed sandstone reservoirs are bounded by shale caprocks, which are cut by growth faults. Clay smears might serve to seal the faults [8], but on the other hand, shallow injection experiments into faults in shale showed five orders of magnitude increase in permeability upon reactivation [19,21]. Finkbeiner et al. [72] suggest that deeply sourced hydrocarbons in a northern Gulf of Mexico reservoir may have migrated upward through shale layers along basin-bounding normal growth faults through a fault valving mechanism. If pressurization from CO_2 injection and storage activates fault valving, the onset of slip and the accompanying increase in permeability might be modeled using a variant of the 2D solution presented here. The 2D approximation is relevant if the fault and pressurization extend somewhat uniformly along strike, and a constant pressure "injection" condition is warranted if the reservoir storage capacity is sufficiently large that the reservoir pressure decrease from fluid loss is negligible over the timescales of crack growth through the caprock layer. The primary modification that is needed is to replace bilateral with unilateral crack growth, which will reduce the amount of slip and crack growth relative to the bilateral solution.

We also remark that it would be straightforward to extend our model to allow for pressure diffusion ahead of the crack edge, but with different transport properties. The left side of the edge condition (2.4) would include an additional term describing the fluid flow into the fault zone ahead of the crack edge. The diffusion equation, with different parameters, would also be solved ahead of the crack edge, so the modified edge condition, plus continuity of the pressure change, would be used to couple the solutions behind and ahead of the crack edge. This extension will

introduce two additional dimensionless parameters (the ratio of permeability ahead and behind the crack edge and a similar ratio of specific storage). One limit of this problem (permeability and specific storage ratios equal to unity) would correspond to the Bhattacharya & Viesca [35] and Sáez et al. [49] solutions; another (permeability ratio equal to zero) would correspond to our new solution. An additional extension would allow the injected fluid to have different properties than the fluid that occupies the pore space prior to injection (e.g., injection of CO_2 into a water or brine-filled reservoir). This will add a fluid interface across which Darcy velocity and pressure will be continuous. We anticipate that in most cases, this region would be sufficiently small and hence of low storage capacity relative to the crack, such that there would be minimal differences from the solutions presented in this study.

Finally, recent work by Viesca [73] provides the mathematical foundation to calculate additional features of our new solutions. These would include expressions for slip and seismic moment, in the asymptotic limits we studied, which might be used for model calibration using measurements of slip (e.g., from borehole monitoring or casing deformation).

7. Conclusion

In this study we derived 2D and 3D solutions for fluid-driven shear cracks, which differ from the previous solutions of Bhattacharya & Viesca [35] and Sáez et al. [49] by accounting for permeability enhancement and dilatancy. Both processes were assumed to occur instantaneously at the crack edge. Dilatancy hinders crack growth, preventing the crack from expanding beyond the hydraulic diffusion length set by the fluid transport properties within the crack, even in the critically stressed limit. We provide a closed form solution for the maximum crack growth speed as a function of the dimensionless dilatancy parameter in equation (4.15). Our work also demonstrates how the confinement of flow to the interior, slipped part of the crack (with relatively impermeable conditions ahead of the crack) increases pressurization for constant rate injection. That pressurization is always sufficient to bring the fault to failure (at least if hydraulic fracturing conditions are not met first). This may help explain some observations of fluid-driven crack growth occurring even for severely understressed conditions.

Acknowledgements. This work was motivated by discussions with affiliates of the Stanford Center for Induced and Triggered Seismicity (SCITS).

Funding

This work was funded by the National Science Foundation (EAR-1947448).

Data accessibility

MATLAB scripts to reproduce all figures are available at https://github.com/ericmdunham/fluid-driven-aseismic-slip and https://zenodo.org/doi/10.5281/zenodo.10895689.

References

1. Zoback MD, Kohli A, Das I, McClure M. 2012 The importance of slow slip on faults during hydraulic fracturing stimulation of shale gas reservoirs. In *SPE Unconventional Resources Conference/Gas Technology Symposium* pp. SPE–155476. SPE. (10.2118/155476-MS)
2. McClure MW, Horne RN. 2014 An investigation of stimulation mechanisms in Enhanced Geothermal Systems. *International Journal of Rock Mechanics and Mining Sciences* **72**, 242–260. (10.1016/j.ijrmms.2014.07.011)
3. Norbeck JH, McClure MW, Horne RN. 2018 Field observations at the Fenton Hill enhanced geothermal system test site support mixed-mechanism stimulation. *Geothermics* **74**, 135–149. (10.1016/j.geothermics.2018.03.003)
4. Eaton DW, Eyre TS. 2022 Implications of slow fault slip for hydraulic-fracturing-induced seismicity. *The Leading Edge* **41**, 748–755. (10.1190/tle41110748.1)

5. Zhang F, Jiang Z, Chen Z, Yin Z, Tang J. 2020 Hydraulic fracturing induced fault slip and casing shear in Sichuan Basin: A multi-scale numerical investigation. *Journal of Petroleum Science and Engineering* **195**, 107797. (10.1016/j.petrol.2020.107797)
6. Cappa F, Rutqvist J. 2011 Modeling of coupled deformation and permeability evolution during fault reactivation induced by deep underground injection of CO2. *International Journal of Greenhouse Gas Control* **5**, 336–346. (10.1016/j.ijggc.2010.08.005)
7. Paluszny A, Graham CC, Daniels KA, Tsaparli V, Xenias D, Salimzadeh S, Whitmarsh L, Harrington JF, Zimmerman RW. 2020 Caprock integrity and public perception studies of carbon storage in depleted hydrocarbon reservoirs. *International Journal of Greenhouse Gas Control* **98**, 103057. (10.1016/j.ijggc.2020.103057)
8. Silva JA, Saló-Salgado L, Patterson J, Dasari GR, Juanes R. 2023 Assessing the viability of CO2 storage in offshore formations of the Gulf of Mexico at a scale relevant for climate-change mitigation. *International Journal of Greenhouse Gas Control* **126**, 103884. (10.1016/j.ijggc.2023.103884)
9. Kohli AH, Zoback MD. 2013 Frictional properties of shale reservoir rocks. *Journal of Geophysical Research: Solid Earth* **118**, 5109–5125. (10.1002/jgrb.50346)
10. Wynants-Morel N, Cappa F, De Barros L, Ampuero JP. 2020 Stress perturbation from aseismic slip drives the seismic front during fluid injection in a permeable fault. *Journal of Geophysical Research: Solid Earth* **125**, e2019JB019179. (10.1029/2019JB019179)
11. Duboeuf L, De Barros L, Kakurina M, Guglielmi Y, Cappa F, Valley B. 2021 Aseismic deformations perturb the stress state and trigger induced seismicity during injection experiments. *Geophysical Journal International* **224**, 1464–1475. (10.1093/gji/ggaa515)
12. Danré P, De Barros L, Cappa F, Ampuero JP. 2022 Prevalence of aseismic slip linking fluid injection to natural and anthropogenic seismic swarms. *Journal of Geophysical Research: Solid Earth* **127**, e2022JB025571. (10.1029/2022JB025571)
13. Eyre TS, Zecevic M, Salvage RO, Eaton DW. 2020 A long-lived swarm of hydraulic fracturing-induced seismicity provides evidence for aseismic slip. *Bulletin of the Seismological Society of America* **110**, 2205–2215. (10.1785/0120200107)
14. Eyre TS, Eaton DW, Garagash DI, Zecevic M, Venieri M, Weir R, Lawton DC. 2019 The role of aseismic slip in hydraulic fracturing–induced seismicity. *Science Advances* **5**, eaav7172. (10.1126/sciadv.aav7172)
15. Pepin KS, Ellsworth WL, Sheng Y, Zebker HA. 2022 Shallow aseismic slip in the Delaware basin determined by Sentinel-1 InSAR. *Journal of Geophysical Research: Solid Earth* **127**, e2021JB023157. (10.1029/2021JB023157)
16. Eyre TS, Samsonov S, Feng W, Kao H, Eaton DW. 2022 InSAR data reveal that the largest hydraulic fracturing-induced earthquake in Canada, to date, is a slow-slip event. *Scientific Reports* **12**, 2043. (10.1038/s41598-022-06129-3)
17. Guglielmi Y, Cappa F, Avouac JP, Henry P, Elsworth D. 2015 Seismicity triggered by fluid injection–induced aseismic slip. *Science* **348**, 1224–1226. (10.1126/science.aab0476)
18. Cappa F, Scuderi MM, Collettini C, Guglielmi Y, Avouac JP. 2019 Stabilization of fault slip by fluid injection in the laboratory and in situ. *Science Advances* **5**, eaau4065. (10.1126/sciadv.aau4065)
19. Guglielmi Y, Nussbaum C, Cappa F, De Barros L, Rutqvist J, Birkholzer J. 2021 Field-scale fault reactivation experiments by fluid injection highlight aseismic leakage in caprock analogs: Implications for CO2 sequestration. *International Journal of Greenhouse Gas Control* **111**, 103471. (10.1016/j.ijggc.2021.103471)
20. Cappa F, Guglielmi Y, De Barros L. 2022a Transient evolution of permeability and friction in a slowly slipping fault activated by fluid pressurization. *Nature Communications* **13**, 3039. (10.1038/s41467-022-30798-3)
21. Cappa F, Guglielmi Y, Nussbaum C, De Barros L, Birkholzer J. 2022b Fluid migration in low-permeability faults driven by decoupling of fault slip and opening. *Nature Geoscience* **15**, 747–751. (10.1038/s41561-022-00993-4)
22. Marone C, Raleigh CB, Scholz C. 1990 Frictional behavior and constitutive modeling of simulated fault gouge. *Journal of Geophysical Research: Solid Earth* **95**, 7007–7025. (10.1029/JB095iB05p07007)
23. Lockner DA, Byerlee JD. 1994 Dilatancy in hydraulically isolated faults and the suppression of instability. *Geophysical Research Letters* **21**, 2353–2356. (10.1029/94GL02366)
24. Samuelson J, Elsworth D, Marone C. 2009 Shear-induced dilatancy of fluid-saturated faults: Experiment and theory. *Journal of Geophysical Research: Solid Earth* **114**. (10.1029/2008JB006273)

25. Brantut N. 2020 Dilatancy-induced fluid pressure drop during dynamic rupture: Direct experimental evidence and consequences for earthquake dynamics. *Earth and Planetary Science Letters* **538**, 116179. (10.1016/j.epsl.2020.116179)
26. Proctor B, Lockner D, Kilgore B, Mitchell T, Beeler N. 2020 Direct evidence for fluid pressure, dilatancy, and compaction affecting slip in isolated faults. *Geophysical Research Letters* **47**, e2019GL086767. (10.1029/2019GL086767)
27. Aben FM, Brantut N. 2021 Dilatancy stabilises shear failure in rock. *Earth and Planetary Science Letters* **574**, 117174. (10.1016/j.epsl.2021.117174)
28. Brantut N. 2021 Dilatancy toughening of shear cracks and implications for slow rupture propagation. *Journal of Geophysical Research: Solid Earth* **126**, e2021JB022239. (10.1029/2021JB022239)
29. Lee H, Cho T. 2002 Hydraulic characteristics of rough fractures in linear flow under normal and shear load. *Rock Mechanics and Rock Engineering* **35**, 299–318. (10.1007/s00603-002-0028-y)
30. Im K, Elsworth D, Wang C. 2019 Cyclic permeability evolution during repose then reactivation of fractures and faults. *Journal of Geophysical Research: Solid Earth* **124**, 4492–4506. (10.1029/2019JB017309)
31. Almakari M, Chauris H, Passelègue F, Dublanchet P, Gesret A. 2020 Fault's hydraulic diffusivity enhancement during injection induced fault reactivation: application of pore pressure diffusion inversions to laboratory injection experiments. *Geophysical Journal International* **223**, 2117–2132. (10.1093/gji/ggaa446)
32. Ji Y, Zhang W, Hofmann H, Cappa F, Zhang S. 2023 Fracture permeability enhancement during fluid injection modulated by pressurization rate and surface asperities. *Geophysical Research Letters* **50**, e2023GL104662. (10.1029/2023GL104662)
33. Segall P, Rice JR. 1995 Dilatancy, compaction, and slip instability of a fluid-infiltrated fault. *Journal of Geophysical Research: Solid Earth* **100**, 22155–22171. (10.1029/95JB02403)
34. Segall P, Rubin AM, Bradley AM, Rice JR. 2010 Dilatant strengthening as a mechanism for slow slip events. *Journal of Geophysical Research: Solid Earth* **115**. (10.1029/2010JB007449)
35. Bhattacharya P, Viesca RC. 2019 Fluid-induced aseismic fault slip outpaces pore-fluid migration. *Science* **364**, 464–468. (10.1126/science.aaw735)
36. Larochelle S, Lapusta N, Ampuero JP, Cappa F. 2021 Constraining fault friction and stability with fluid-injection field experiments. *Geophysical Research Letters* **48**, e2020GL091188. (10.1029/2020GL091188)
37. Dvory NZ, Yang Y, Dunham EM. 2022 Models of injection-induced aseismic slip on height-bounded faults in the Delaware Basin constrain fault-zone pore pressure changes and permeability. *Geophysical Research Letters* **49**, e2021GL097330. (10.1029/2021GL097330)
38. Dublanchet P. 2019 Fluid driven shear cracks on a strengthening rate-and-state frictional fault. *Journal of the Mechanics and Physics of Solids* **132**, 103672. (10.1016/j.jmps.2019.07.015)
39. Viesca RC. 2021 Self-similar fault slip in response to fluid injection. *Journal of Fluid Mechanics* **928**, A29. (10.1017/jfm.2021.825)
40. Sáez A, Lecampion B. 2023 Fluid-driven slow slip and earthquake nucleation on a slip-weakening circular fault. *Journal of the Mechanics and Physics of Solids* p. 105506. (10.1016/j.jmps.2023.105506)
41. Alghannam M, Juanes R. 2020 Understanding rate effects in injection-induced earthquakes. *Nature Communications* **11**, 3053. (10.1038/s41467-020-16860-y)
42. Zhang Y, Schaubs P, Zhao C, Ord A, Hobbs B, Barnicoat A. 2008 Fault-related dilation, permeability enhancement, fluid flow and mineral precipitation patterns: numerical models. *Geological Society, London, Special Publications* **299**, 239–255. (10.1144/SP299.15)
43. Ciardo F, Lecampion B. 2019 Effect of dilatancy on the transition from aseismic to seismic slip due to fluid injection in a fault. *Journal of Geophysical Research: Solid Earth* **124**, 3724–3743. (10.1029/2018JB016636)
44. Yang Y, Dunham EM. 2021 Effect of porosity and permeability evolution on injection-induced aseismic slip. *Journal of Geophysical Research: Solid Earth* **126**, e2020JB021258. (10.1029/2020JB021258)
45. Parez S, Kozakovic M, Havlica J. 2023 Pore pressure drop during dynamic rupture and conditions for dilatancy hardening. *Journal of Geophysical Research: Solid Earth* **128**, e2023JB026396. (10.1029/2023JB026396)
46. Sibson RH. 1992 Fault-valve behavior and the hydrostatic-lithostatic fluid pressure interface. *Earth-Science Reviews* **32**, 141–144. (10.1016/0012-8252(92)90019-P)

47. Cox SF. 2005 Coupling between deformation, fluid pressures, and fluid flow in ore-producing hydrothermal systems at depth in the crust. *Economic Geology; Bulletin of the Society of Economic Geologists* **100**, 39–75.
48. Zhu W, Allison KL, Dunham EM, Yang Y. 2020 Fault valving and pore pressure evolution in simulations of earthquake sequences and aseismic slip. *Nature Communications* **11**, 4833. (10.1038/s41467-020-18598-z)
49. Sáez A, Lecampion B, Bhattacharya P, Viesca RC. 2022 Three-dimensional fluid-driven stable frictional ruptures. *Journal of the Mechanics and Physics of Solids* **160**, 104754. (10.1016/j.jmps.2021.104754)
50. Caine JS, Evans JP, Forster CB. 1996 Fault zone architecture and permeability structure. *Geology* **24**, 1025–1028. (10.1130/0091-7613(1996)024<1025:FZAAPS>2.3.CO;2)
51. Wibberley CA. 2002 Hydraulic diffusivity of fault gouge zones and implications for thermal pressurization during seismic slip. *Earth, Planets and Space* **54**, 1153–1171. (10.1186/BF03353317)
52. Faulkner D, Jackson C, Lunn R, Schlische R, Shipton Z, Wibberley C, Withjack M. 2010 A review of recent developments concerning the structure, mechanics and fluid flow properties of fault zones. *Journal of Structural Geology* **32**, 1557–1575. (10.1016/j.jsg.2010.06.009)
53. Ciardo F, Lecampion B. 2023 Injection-induced aseismic slip in tight fractured rocks. *Rock Mechanics and Rock Engineering* pp. 1–22. (10.1007/s00603-023-03249-8)
54. Mavko G, Mukerji T, Dvorkin J. 2020 *The Rock Physics Handbook*. Cambridge University Press.
55. Dal Zilio L, Hegyi B, Behr W, Gerya T. 2022 Hydro-mechanical earthquake cycles in a poro-visco-elasto-plastic fluid-bearing fault structure. *Tectonophysics* **838**, 229516. (10.1016/j.tecto.2022.229516)
56. Yang Y, Dunham EM. 2023 Influence of creep compaction and dilatancy on earthquake sequences and slow slip. *Journal of Geophysical Research: Solid Earth* **128**, e2022JB025969. (10.1029/2022JB025969)
57. Broberg KB. 1999 *Cracks and Fracture*. Academic Press.
58. Garagash DI. 2021 Fracture mechanics of rate-and-state faults and fluid injection induced slip. *Philosophical Transactions of the Royal Society A* **379**, 20200129. (10.1098/rsta.2020.0129)
59. Lai YS, Movchan AB, Rodin GJ. 2002 A study of quasi-circular cracks. *International Journal of Fracture* **113**, 1–25. (10.1023/A:1013712515461)
60. Sáez A, Lecampion B. 2023 Post-injection aseismic slip as a mechanism for the delayed triggering of seismicity. *Proceedings of the Royal Society A* **479**, 20220810. (10.1098/rspa.2022.0810)
61. Sáez A, Lecampion B. 2024 Fluid-driven slow slip and earthquake nucleation on a slip-weakening circular fault. *Journal of the Mechanics and Physics of Solids* **183**, 105506. (10.1016/j.jmps.2023.105506)
62. Humphreys B, Hodson-Clarke A, Hogarth R. 2014 Habanero geothermal project field development plan. *Geodynamics Ltd.: Brisbane, Australia*.
63. Baisch S, Weidler R, Vörös R, Wyborn D, de Graaf L. 2006 Induced seismicity during the stimulation of a geothermal HFR reservoir in the Cooper Basin, Australia. *Bulletin of the Seismological Society of America* **96**, 2242–2256. (10.1785/0120050255)
64. Baisch S, Vörös R, Weidler R, Wyborn D. 2009 Investigation of fault mechanisms during geothermal reservoir stimulation experiments in the Cooper Basin, Australia. *Bulletin of the Seismological Society of America* **99**, 148–158. (10.1785/0120080055)
65. Baisch S, Rothert E, Stang H, Vörös R, Koch C, McMahon A. 2015 Continued geothermal reservoir stimulation experiments in the Cooper Basin (Australia). *Bulletin of the Seismological Society of America* **105**, 198–209. (10.1785/0120140208)
66. Baisch S. 2020 Inferring in situ hydraulic pressure from induced seismicity observations: An application to the Cooper Basin (Australia) geothermal reservoir. *Journal of Geophysical Research: Solid Earth* **125**, e2019JB019070. (10.1029/2019JB019070)
67. Barton C, Moos D, Hartley L, Baxter S, Foulquier L, Holl H, Hogarth R, Brisbane A. 2013 Geomechanically coupled simulation of flow in fractured reservoirs. In *Proceedings 38th Workshop on Geothermal Reservoir Engineering, Stanford University, Stanford, California, February* pp. 11–13.
68. Holl HG, Barton C. 2015 Habanero field-structure and state of stress. In *Proceedings World Geothermal Congress* pp. 19–25.
69. Wang TA, Dunham EM. 2022 Hindcasting injection-induced aseismic slip and microseismicity

at the Cooper Basin Enhanced Geothermal Systems Project. *Scientific Reports* **12**, 19481. (10.1038/s41598-022-23812-7)
70. Garagash DI, Germanovich LN. 2012 Nucleation and arrest of dynamic slip on a pressurized fault. *Journal of Geophysical Research: Solid Earth* **117**. (10.1029/2012JB009209)
71. Galis M, Ampuero JP, Mai PM, Cappa F. 2017 Induced seismicity provides insight into why earthquake ruptures stop. *Science Advances* **3**, eaap7528. (10.1126/sciadv.aap7528)
72. Finkbeiner T, Zoback M, Flemings P, Stump B. 2001 Stress, pore pressure, and dynamically constrained hydrocarbon columns in the South Eugene Island 330 field, northern Gulf of Mexico. *AAPG Bulletin* **85**, 1007–1031. (10.1306/8626CA55-173B-11D7-8645000102C1865D)
73. Viesca RC. 2024 Asymptotic solutions for self-similar fault slip induced by fluid injection at constant rate. (10.48550/arXiv.2401.13828)